Port, A.; Gurgel, K.-W.; Staneva, J.; Schulz-Stellenfleth, J.; Stanev, E.V.:
Tidal and wind-driven surface currents in the German Bight: HFR observations versus model simulations
In: Ocean Dynamics (2011) Springer

DOI: 10.1007/s10236-011-0412-9

manuscript No.
(will be inserted by the editor)

Tidal and wind-driven surface currents in the German Bight: HFR observations versus model simulations

Alexander Port · Klaus-Werner Gurgel · Joanna Staneva · Johannes Schulz-Stellenfleth · Emil Stanev

Received: date / Accepted: date

Abstract Coastal high-frequency radar (HFR) observations of surface currents in the German Bight and hindcasts from a primitive equation numerical model were examined with respect to tidal and wind-driven components. The region of interest lies between the shallow mudflats of the North Frisian islands and the island of Helgoland 50 km offshore, with water depths ranging from less than 5 m to approximately 30 m. HFR observation data cover six months from August 1991 to February 1992. Measurements with a coherent integration time of 18 minutes were repeated every 30 minutes. Based on signals from two radar sites, zonal and meridional velocities are available at a horizontal resolution of 3 km. The numerical model domain covers the region of interest as well as the surrounding German Bight with a horizontal resolution of 1 km and a vertical resolution of 21 layers in sigma coordinates, of which only the surface layer was used for the analyses.

The month of September 1991 was chosen for detailed comparisons. A tidal harmonic analysis was applied to extract the dominant tidal components and to obtain corresponding tidal ellipses. Complex correlation coefficients between HFR surface currents and wind were calculated to illustrate the regional importance of wind forcing. The same analysis has been applied to the numerically simulated currents.

Good agreement between analysis results based on HFR and model data can be found especially for mesoscale spatial patterns of tidal ellipse orientation and complex correlation between wind and surface current. This agreement gives credibility to sensitivity analyses carried out with the aim to quantify the contribution of different forcing mechanisms to regional dynamics. We demonstrated that the change of the correlation patterns between wind and surface current from the coastal to open ocean are not only due to density. The effect of coastal line and topography are quite pronounced as well. Conclusion is that unlike many other remote sensing data HFR observations resolve these effects. Therefore they could present an important component for regional operational oceanography.

Keywords radar · HFR · wind-driven currents · tidal currents · tidal analysis · complex correlation · coastal oceanography

Alexander Port
ICBM, University of Oldenburg, Germany
E-mail: alexander.port@uni-oldenburg.de

Klaus-Werner Gurgel
Institute of Oceanography, University of Hamburg, Germany

Joanna Staneva · Emil Stanev · Johannes Schulz-Stellenfleth
Institute for Coastal Research, GKSS Research Centre, Germany

1 Introduction

High Frequency (HF) radars are operated in the decameter range of radio frequencies and provide remotely sensed area covering data sets of surface currents. Depending on the operating frequency, the measurements can reach ranges up to 200 km along the ocean surface, covering thousands of square kilometers. In contrast to satellites, which pass a location every couple of days, an HF radar can monitor an area of interest continuously at sampling rates down to a few minutes.

Currently, ocean monitoring systems are installed along selected coastal areas world wide, implementing an approach which combines measurements and models by data assimilation. The measurements help the model by providing more information on boundary conditions, resulting in model data which are closer to the actual

situation and allowing more accurate predictions. Before combining measurements and models, investigations on data quality and model statistics are necessary to check if the measurement errors are small enough to support the model, and if major processes found in the measurements have been well captured by the model.

The area of interest in this study, which is the German Bight, is situated in the Southern North Sea (figure 1) bounded by the Netherlands and Germany to the south, and Denmark and Germany to the east. This is a shallow coastal area with a rectangular geometry, limited by the zonal direction of the coast line towards Holland and the meridional direction towards Denmark. An extension of the Elbe Estuary towards the north-west can be seen in the bathymetry. A Kelvin wave following the coast changes direction, as well as the residual currents.

It is well known that the sense of rotation of tidal ellipses is principally determined by the relative strength of Coriolis force, sea-surface pressure gradients and bottom friction. Taylor's theoretical calculations for a rectangular basin suggest positive ellipticity in the German Bight. However, it is not only the induction of ellipticity by geometry which can be considerable. Bathymetric gradients are another source of ellipticity changes. Furthermore, the shallow German Bight is a transition area where dominating balances change from geostrophy to friction domination, therefore changes in the rotation can also be expected.

Most of the fresh water input for the German Bight, which is due to Elbe and Weser Rivers, is also located in the south-eastern corner, making dynamics there extremely complex. It is therefore expected that the influence of geometry (including topography) and stratification (dominated by inputs of freshwater), will control the local dynamics there. Internal friction could also play an important role, which has been demonstrated by Carbajal and Pohlmann (2004) claiming that baroclinic effects significantly modify the inclination of tidal ellipses.

The German Bight has been addressed in numerous studies dealing with observations and numerical modelling. Two of them, Schirmer et al. (1994) and Carbajal and Pohlmann (2004), could be considered as precursors of the present paper. The former study estimated tidal ellipses for different tidal constituents from CODAR measurements carried out in the German Bight showing clearly that the input of freshwater and, in general, baroclinic effects favored CW rotation in this region. The major changes occurred in the neighbourhood of the openings of the embayments. According to Carbajal and Pohlmann (2004) in the German Bight, stratification produces negative ellipticity almost everywhere. These results are relevant to independent analyses linking the line separating cyclonic and anticyclonic rotation with the position of the thermal front that divides well-mixed and stratified regions (Czitrom et al., 1988). According to Soulsby (1983) the boundary between the CW and AC component of the flow could be, in some cases, a good indication of thermal fronts. In the case of the German Bight it is the haline front which is more important, in particular in the south-eastern corner, which is the major area of our interest.

The main objective of this paper is to analyse a data set of surface currents acquired by HF radar in the German Bight from August 9th 1991 to February 4th 1992 and to compare it to ocean currents given by a state-of-the-art numerical hydrodynamical model (GETM, Burchard and Bolding, 2002).

Although it is well known that the processes driving the circulation in the German Bight are dominated by tides, wind, and fresh water inflow from the rivers Elbe and Weser, the regional impact of wind forcing has not been enough considered. Following the linear Ekman theory one could expect that surface currents and wind should well be correlated. However, the problem is not so trivial because Ekman theory is valid for an infinite ocean. It is not only the presence of coast which is crucial in our case, but also the change of its orientation. Additionally, the fresh water flux is located in the corner of the Bight. One could thus expect that the correlation between wind and surface current will be weaker. Demonstrating this effect is one of the major tasks of the present study. The second one is to revisit some issues addressed by Schirmer et al. (1994) and Carbajal and Pohlmann (2004), such as tidal characteristics, using HFR data and finer resolution numerical model, with up-to-date physical parameterizations.

The paper is structured as follows. We first address in section 2 available data from observations and numerical simulations, as well as methods used to analyse them. Preparatory analysis of simulated circulation patterns in the German Bight is presented in section 3. Section 4 deals with model data intercomparison, followed by a general discussion of results and conclusions.

2 Data sources and analysis methods

2.1 HFR observations

Within a German national research project ("PRISMA", BMFT-Projekt 03F0558A1; PRISMA, 1994), the University of Hamburg had installed two HFRs, one on the mainland coast near to the town of St. Peter-Ording at 54.34° N, 8.59° E, and one on the island Helgoland

at 54.19° N, 7.88° E, about 50 km offshore in the German Bight. The greater region of interest is shown in figure 1, with bathymetry information as used in the hydrodynamical model setup, while figure 2 shows the locations and the area covered by both HFRs. The working range of the systems is typical of the operating frequency choosen.

The HFRs used within "PRISMA" were based on an early CODAR ("Coastal Ocean Dynamics Applications Radar") design developed at NOAA (Barrick et al., 1977) and had been modified at the University of Hamburg. The systems were operated from August of 1991 until February of 1992 to measure surface current velocities. Both HFRs were operated at 29.85 MHz, measuring the radial component of the surface current averaged over a layer extending to approximately 0.5 m below the sea surface. These radial components were combined to give estimates of zonal and meridional surface velocity together with corresponding observation error estimates on a horizontal cartesian grid with 3 km resolution. Every 30 minutes, data collected over 18 minutes of "coherent integration time" (CIT) was processed to produce one sample in time.

The observation error estimate consists of two major components: The error of the radial surface current, which includes current variability within the CIT, and a factor describing the influence due to geometry called "Geometric Dilution Of Precision" (GDOP, Chapman et al., 1997). The GDOP is well known from the satellite-based "Global Positioning System" (GPS) and has exactly the same meaning in this context. Details are discussed by Barth et al. (2010). Figure 3 shows the spatial distribution of the GDOP for the HFR measurement grid. Around the line connecting the two HFRs, high errors related to geometry can be observed (GDOP $\geq$ 5), because the angle between the two radial components becomes too large. In order to reduce these high errors and to avoid gaps in the data set, the radial component from the radar site providing the smaller error, i.e. in most cases the radial component closer to a radar, was selected and the current velocity perpendicular to the radial component was interpolated from the neighbouring grid cells. These measured and interpolated values were then combined to give the 2-dimensional surface current. A similar approach was used to compute the observation error estimates.

Figure 4 shows the mean observation error over 6 months calculated from the error of the radial components or in case of GDOP $\geq$ 5 estimated using the interpolation procedure described above. As a result, the errors around the baseline connecting the two HFR system locations are much smaller than the GDOP values given in figure 3 suggest. Some influence of the geometry on the measurement error can still be seen in the meridional component.

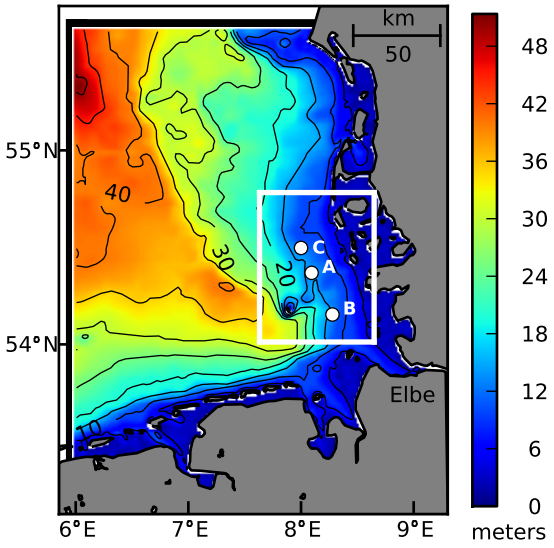

Fig. 1 The hydrodynamical model domain covers the German Bight, with open boundaries to the north and west of the North Sea (broad black lines). Bathymetry as used in the model setup is shown in meters, color-coded according to the colorbar. The rectangular white inset outlines the HFR observation grid domain as used in the corresponding figures. The island of Helgoland is located in the south-west corner of this inset, with a relatively shallow area visible east-north-east of it. The Elbe river outflow enters the German Bight close to the HFR observation grid from the south-east. Locations A and B (white circles) indicate exemplary grid points as used for time series examples in figure 10. The two locations were chosen as a compromise between high coverage over time (see figure 2) and low GDOP (see figure 3), one north and one south of the baseline connecting the two HFR systems. ECMWF wind timeseries from location C were used for complex correlation analysis.

For purposes of tidal and complex correlation analyses, only those points on the observation grid were included where the coverage over time of the HFR observations is at least 50% and the water depth at least 5 m (the latter criterion was also applied to model simulation data).

2.2 Numerical simulations

Numerical simulations were performed using the 3D primitive equation General Estuarine Transport Model (GETM, Burchard and Bolding, 2002). The nested-grid model consists of a coarse-resolution North Sea-Baltic Sea (3 nautical miles) outer model, and a nested German Bight model with a horizontal resolution of about 1 km. Both models have 21 layers in generalized coordinates. The horizontal discretization is done on a

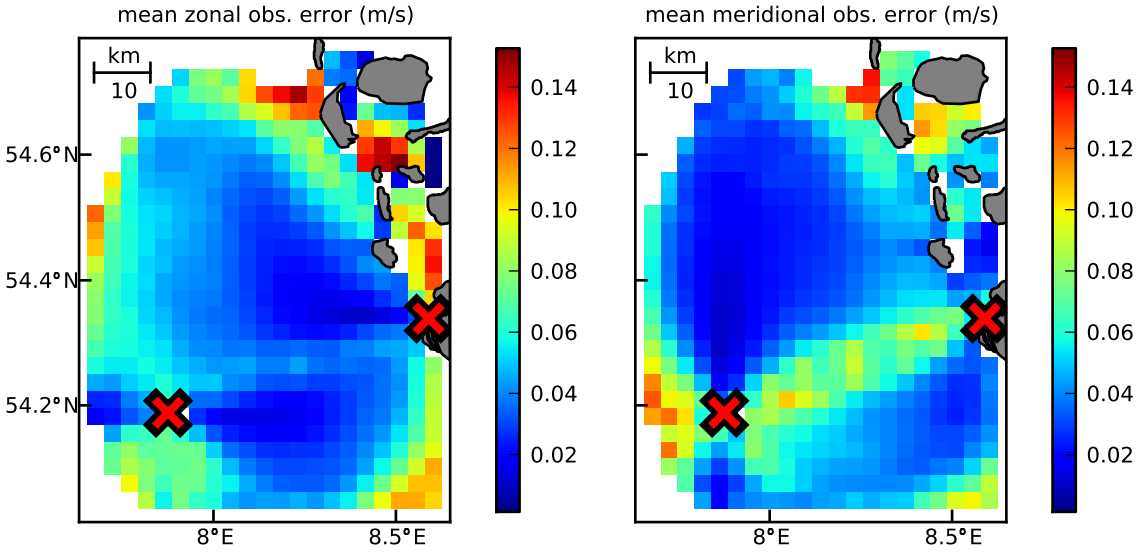

Fig. 4 HFR observation error estimates: at each grid point, the mean over time for the entire time series (8414 samples for observation grid points with full coverage over time) is shown separately for the zonal (left panel) and meridional (right panel) component (color-coded according to the colorbars, identical scales).

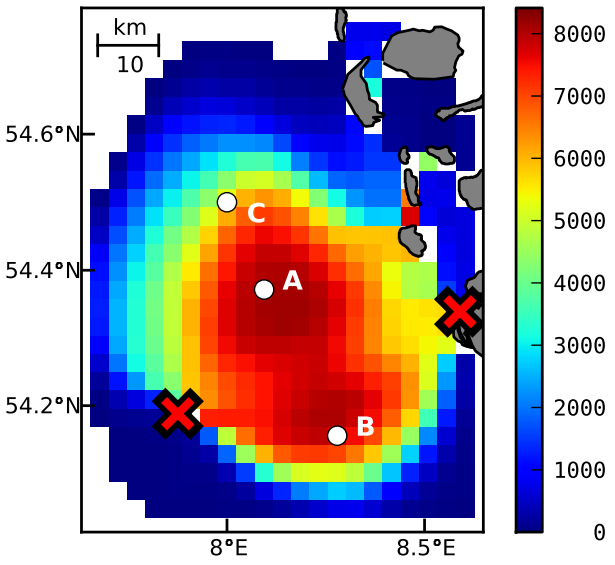

Fig. 2 Temporal coverage of the HFR surface velocity observations: the number of samples available at each grid point is color-coded according to the colorbar, the entire dataset (6 months) comprising 8414 samples in time. The data collected during September 1991 was extracted for further analyses. Islands in the north-east and east as well as the mainland coast in the east are shown in gray, the HFR system locations are indicated by red-on-black crosses: the western location on the island of Helgoland (occluded at this scale) and the eastern location near the village of St. Peter-Ording. Locations A, B and C are reproduced from figure 1.

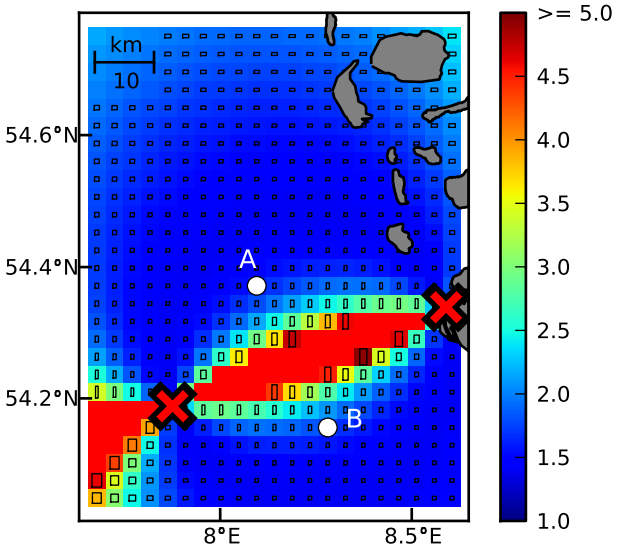

Fig. 3 The spatial distribution of the observation error due to geometry. The boxes' height and width indicate the north and east components of GDOP, the color scale gives the absolute value. Locations A and B are reproduced from figure 1.

spherical grid. The bathymetric data for both models are prepared using the ETOPO-1 topography, together with observations made available from the German Hydrographic Service (Bundesamt fuer Seeschiffahrt und Hydrographie, BSH; Dick et al., 2001). The bathymetry

as well as the northern and western open boundaries used by the hydrodynamic model are shown in figure 1.

The model system is forced by: (1) The meteorological forcing derived from bulk formulae using six-hourly reanalysis data, including wind (exemplary wind speed and vector orientation for 1991/09 is shown in figure 5), mean sea level pressure, air temperature, humidity and cloud cover on a 0.5° by 0.5° grid from the European Centre for Medium-Range Weather Forecasts (ECMWF); (2) River inflow using climatological data for the 30 most important rivers within the North Sea-Baltic Sea model area provided by the Swedish Meteorological and Hydographical Institute (SMHI); (3) Time varying lateral boundary conditions of sea surface elevations and salinity. The sea surface elevation of the western and northern open boundaries of the German Bight set-up is taken from the North Sea-Baltic Sea model output with five minutes time interval. The tidal forcing at the open boundaries of the North Sea-Baltic Sea model towards the Norwegian Sea and the English Channel was constructed from 13 partial tides from the TOPEX-POSEIDON data set. Temperature and salinity at those open boundaries are interpolated at each time step using the monthly mean climatological data of Janssen et al. (1999). The setup has been described in more detail by Staneva et al. (2009).

For comparisons with HFR observation data and derived analyses, numerical model output was interpolated bilinearly from the surface layer of the 1 km horizontal grid to the HFR observation grid. For purposes of tidal and complex correlation analyses, only those points on the observation grid were included where the water depth is at least 5 m.

To examine the influence of the patterns of availability of observations, i.e., the missing-value mask in time and space, "synthetic observations" were initially also generated: after bilinear interpolation of the model currents to the HFR observation grid, time and location of missing values from the HFR observations were identified and their corresponding model data were discarded. Since the differences in results of the tidal and complex correlation analyses were negligible for the area and tidal constituents discussed here, results based on synthetic observations are not shown separately.

2.3 Tidal analysis

Classical tidal harmonic analysis was performed using t_tide (Pawlowicz et al., 2002), version 1.02 (with minor changes to enable execution under GNU Octave instead of MATLAB). The code was also extended to implement weighted least squares (WLS) in addition to ordinary least squares (OLS) fitting, in order to optionally take into account HFR observation error estimates. For an exemplary grid point (location A, see figure 2), tidal constituent amplitudes with 95% confidence intervals based on numerical simulations as well as HFR observations are shown in figure 6.

For any type of tidal harmonic analysis a finite set of tidal constituents must be chosen. Constituents which are unlikely to be resolved for the given length of the time series may be discarded beforehand. A further possiblity implemented in t_tide is to refine the set based on each constituent's signal-to-noise-ratio (SNR). In this context, SNR refers to the ratio between estimated constituent amplitude and corresponding estimated amplitude error, which is determined in a "first-pass" analysis via bootstrapping (see Pawlowicz et al., 2002, for details). The final synthesised tidal current prediction output would then be calculated by a "second pass" based on the refined set of constituents. Since the tidal analysis is carried out independently for each grid point, it would be straightforward to choose a new set of constituents for each grid point.

Nonetheless, for this specific observation dataset (whose "quality" is highly variable on the grid), we think it is more appropriate to choose a fixed set of constituents to be used for the entire grid in order to avoid confounding changes in the quality of observations with changes in the tidal processes. The selection of constituents to be included was based on an examination of their major axis amplitudes and SNR on the entire grid as well as at a grid point (54.3° N, 8.1° E) of high observation coverage over time and low expected GDOP. The final set of constituents used for the tidal analyses comprises diurnal (O1, K1), semi-diurnal (N2, M2, S2) and higher frequency components (M4, MS4, M6, 2MS6).

Robust fitting for tidal harmonic analysis using an "iteratively reweighted least squares" (IRLS) algorithm is provided by r_t_tide (Leffler and Jay, 2009), which is based on and extends the capabilities of t_tide. Using a Cauchy weighting function and standard tuning constant, the differences in estimates of M2 semi-major axis between the OLS/WLS and IRLS algorithms were on the order of $0.01\,\mathrm{ms}^{-1}$. Since for our specific application, this difference does not justify the application of IRLS, results are discussed only for the OLS/WLS algorithms.

Initial output of tidal analysis results for the time series of two-dimensional vector surface currents is in terms of ellipse parameters, from which corresponding tidal ellipses for each constituent may subsequently be plotted on the observation or model grid.

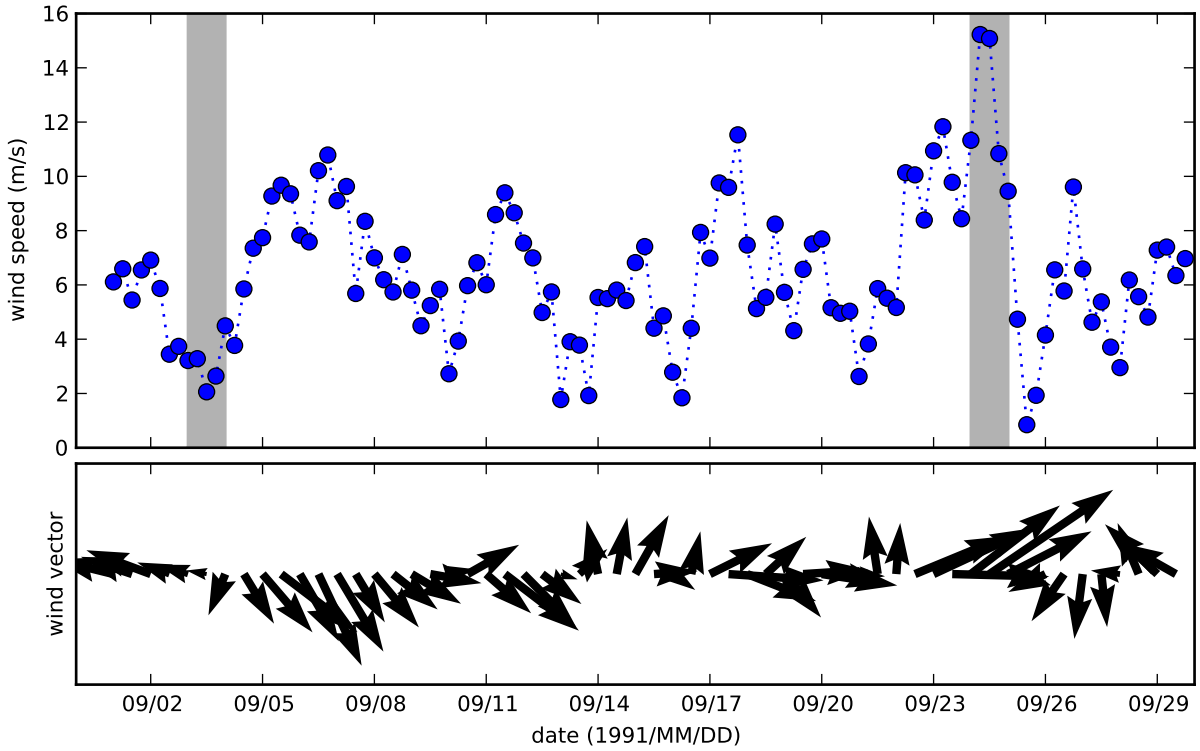

Fig. 5 ECMWF 6-hourly reanalysis surface wind speed data as used for model forcing as well as complex correlation analyses. Wind speed and vector orientation (only every second data point shown for clarity) for 1991/09 are shown from the grid point closest to the middle of the HFR observation grid (54.5° N, 8.0° E; see figure 2, point C). Shaded sections in the upper plot show exemplary (relatively) calm (1991/09/03) and stormy (1991/09/24) days as used for surface current time series examples in figure 10.

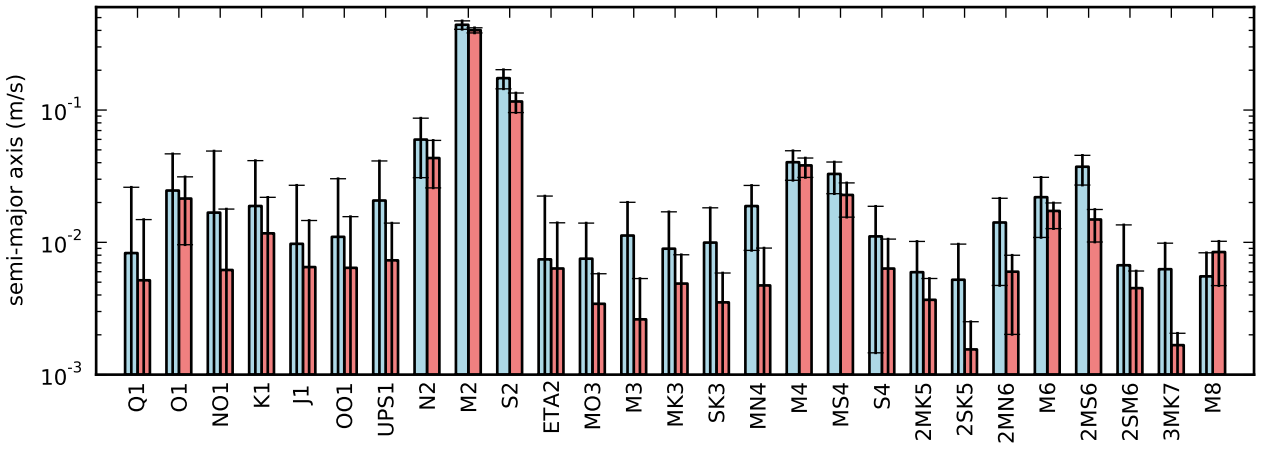

Fig. 6 Tidal constituent amplitudes with 95% confidence intervals from an "unrestricted" tidal analysis based on numerical simulations (blue, left bars) and HFR observations (red, right bars). Data taken from an exemplary grid point (location A, see figure 2) for the month 1991/09. Ordered with increasing frequency from left to right. Constituents with a period longer than 30 h and/or semi-major axis less than 0.001 ms^{-1} are excluded from the figure for clarity. The final set of constituents used for further tidal analyses comprises diurnal (O1, K1), semi-diurnal (N2, M2, S2) and higher frequency components (M4, MS4, M6, 2MS6).

2.4 Wind

To examine the correlation between surface currents and the wind, the complex correlation coefficient ρ (Kundu, 1976) between the time series of two-dimensional surface currents at each grid point of the HFR observation grid and a corresponding time series of the two-dimensional wind field was calculated. Two wind time series were initially examined: one based on local measurements at the eastern HFR system location (St. Peter-Ording) and one extracted from the ECMWF data at the grid point closest to the centre of the HFR observation grid (54.5° N, 8.0° E, , point C in figure 1). In each case, the wind speed U10/V10 at 10 m height was considered. The differences between these two data sources during the period which was further examined (1991/09) did not result in appreciable changes in analysis results. Since the ECMWF data is available continuously, while the local measurements are only available for the HFR observation period (1991/08–1992/02), here we only present results based on ECMWF data to facilitate comparisons with future studies. The ECMWF wind speed and wind vector direction for the aforementioned grid point for 1991/09 is shown in figure 5.

For the surface currents and wind time series, each two-dimensional horizontal vector with zonal component u and meridional component v was converted to a complex vector w:

$$w(t) = u + iv(t). \tag{1}$$

From each surface current vector w_1 and the common wind vector w_2, ρ was calculated as

$$\rho = \frac{\langle w_1^* w_2 \rangle}{\langle w_1^* w_1 \rangle^{\frac{1}{2}} \langle w_2^* w_2 \rangle^{\frac{1}{2}}}, \tag{2}$$

where a superscript star (*) denotes the complex conjugate and $\langle \cdot \rangle$ the arithmetic average over time. This definition is adopted from (Kundu, 1976).

The calculation of ρ was carried out for total currents, "tidal" currents predicted by a synthesis of analysed tidal constituents and non-tidal "residual" currents obtained by subtracting tidal from total currents.

Kundu (1976) used his formulation of the complex correlation coefficient to illustrate the systematic deviation to the left (cyclonic in the northern hemisphere) of currents in the bottom layer compared to the direction of geostrophic velocities. It is noteworthy in the context of the following analyses that he first filtered the data to eliminate effects of tidal oscillations. He demonstrated that the capabilities of classical approaches to evaluate the veering suffer from strongly varying angles (weak currents events increase the uncertainty in veering angle). In equation (2), the denominator normalises corresponding correlations by the dispersions of the velocities. The magnitude $|\rho|$ is informative for the strength of correlation while the phase angle $\arg(\rho)$ illustrates the veering angle, which "is meaningful only if the magnitude of the correlation is high" (Kundu, 1976).

3 German Bight circulation

The circulation of the German Bight has been addressed in numerous studies with a major focus on numerical modelling of tides (Flather, 1976; Maier-Reimer, 1977; Backhaus, 1980; Davies and Furnes, 1980). Numerical simulations of Carbajal and Pohlmann (2004) had approached the state of the art with high enough resolution modelling (1.5 min in the north-south and 2.5 min in the east-west direction) and realistic forcing needed to adequately address similarity between observations and simulations. Recently, operational forecasting performed at the German Hydrographic Service (BSH) has reached high maturity of the fine resolution products (`http://www.bsh.de/aktdat/modell/stroemungen/Modell1.htm`). Furthermore, the work of Staneva et al. (2009) enabled a framework for addressing here the agreement between numerical simulations and HFR observations.

From the earlier studies and present numerical simulations it follows that the wind supports a residual circulation in the direction of propagation of the tidal wave (from west to east along the southern boundary and from south to north along the coasts of Germany and Denmark). Simulations carried out with the numerical model described in section 2.2 demonstrated that the tidal signal associated with the amphidromy at 55.5° N, 5.5° E travels along the coast of the area shown in figure 1 in about three to four hours. Tidal range is from 2.5 m (easternmost and northernmost coastal locations) to about 3.5 m (the Elbe river mouth), which allows the coastal area to be classified as exposed to upper mesotidal conditions.

Figure 7 shows time-averaged surface current, vertically averaged current and vertically integrated transport (vertically averaged current times local depth) for the German Bight during September 1991. This presentation of circulation is needed in order to illustrate the field which we further analyse, that is the surface current (figure 7a), and to give an idea about consistency between surface and vertical mean current or transport. Obviously the three patterns reveal different characteristics of the circulation. It is noteworthy that the surface current has a pronounced maximum along the southern coast and shows a convergence from west to east. Absolute maxima are located in the regions of straits connecting intertidal basins with the open ocean.

Vertically averaged current (figure 7b) is qualitatively similar to the surface current. However, along the western model boundary the meridional component is much stronger. The dominating zonal transport in the surface current in the interior of the model area is substituted by a northward transport in the pattern of vertically averaged current. In both plots the region around the island of Helgoland shows a pronounced regional pattern.

The Eulerian time-mean vertically integrated circulation circulation in most of the German Bight area is cyclonic, which is mainly due to the dominant eastward wind forcing, i.e., a circulation in the direction of propagation of the tidal wave (from west to east along the southern boundary and from south to north along the coasts of Germany and Denmark). A local minimum of the circulation occurs in the coastal East and North Frisian Wadden Sea.

The vertically integrated transport displays to a larger extent the characteristics of the German Bight topography, which is dominated by the underwater extension of the Elbe Estuary. The northern bank of this estuary reduces substantially the penetration of open ocean waters into the shallow coastal zone, and consequently the direction of incoming flow turns abruptly to north-northwest.

The question of the role of density for the circulation in the German Bight has been addressed by Carbajal and Pohlmann (2004); however their work focused primarily on the modification of characteristics of tidal ellipses. We assume that further attention has to be paid to this question, in particular because the region is a typical representative of ROFI. It is still not quite clear what the joint role of wind and density for the regional circulation is. Therefore, along with our main numerical simulation (for brevity "realistic" run), we also performed a simulation with constant temperature and salinity (for brevity "constant density" run). By examining the difference between these two experiments we want to illustrate the motivation for the analyses provided in the remainder of the paper.

We discuss below the correlation between surface current and wind. Two analyses are presented: (1) analysis on the correlation between total current velocity and wind, and (2) analysis of the correlation between non-tidal residual velocity and wind. It appeared that the large variability due to tidal currents make the correlation too weak.

Unlike the theoretical case of Ekman currents, which is applied to an infinitely deep ocean, our model area is a mix of very shallow coastal areas, where the surface current is supposed to follow wind direction and depths bigger than the Ekman depth. The preliminary expec-

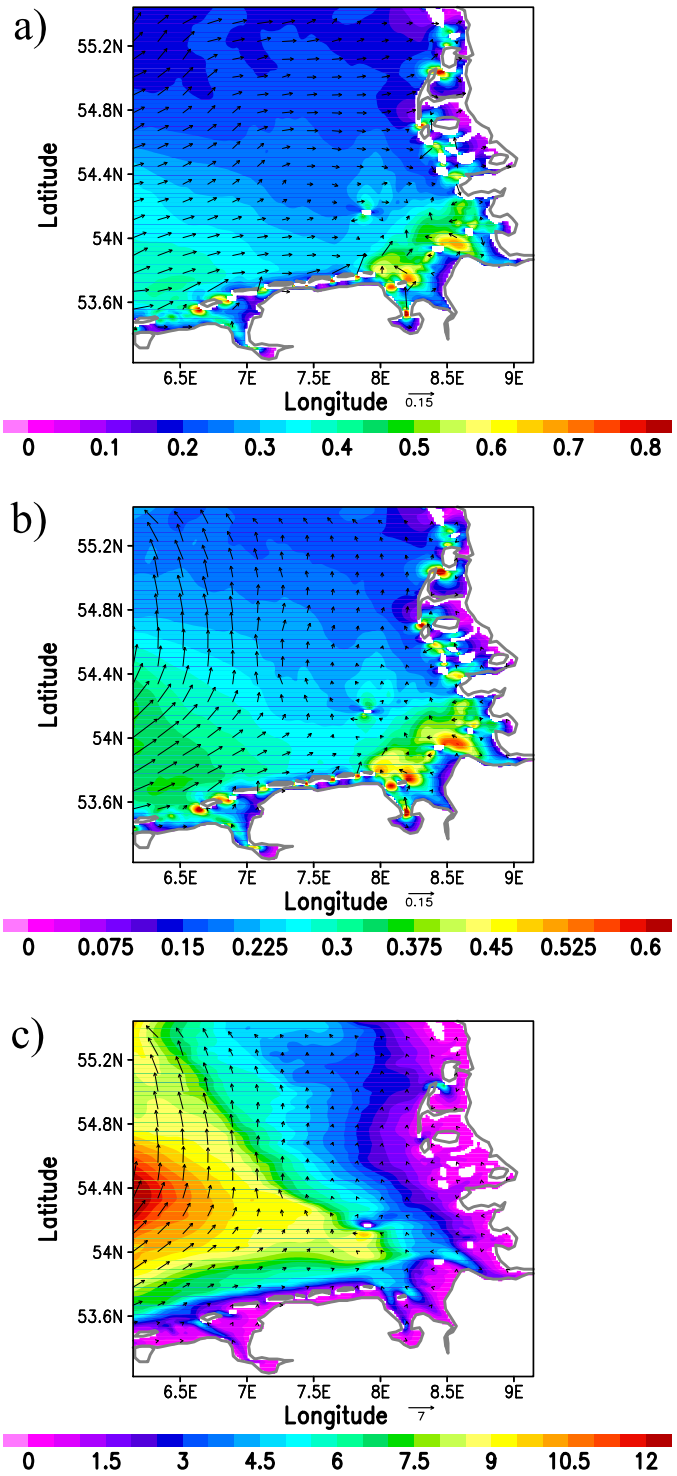

Fig. 7 Eulerian time-mean of currents simulated by the German Bight model for September 1991: a) surface currents (ms^{-1}), b) vertical mean of currents (ms^{-1}) and c) vertically integrated currents (m^2s^{-1}), color-coded according to the colorbars. The arrow below each plot corresponds to current or vertically integrated current in ms^{-1} or m^2s^{-1}, correspondingly.

tation is that the correlation between wind and surface currents will replicate topography changes, however the effects of density are not trivial and difficult to specify in advance.

Analysis of the realistic and constant density runs is presented below first by the complex correlation between the difference of surface velocities in the two experiments and wind (figure 8a). The result is not trivial. It appears that the effect of density results in an increase in the magnitude of complex correlation in an area around the island of Helgoland and extending to the northern model boundary, while changes are minimal in the shallow coastal areas and in the south-west of the domain. As demonstrated by additional analyses of individual velocity components (data not shown) this result is mostly due to meridional velocity.

Subtracting the tidal prediction, the non-tidal residual surface currents show a high correlation with wind (figure 8b and 8c). It is noteworthy that low magnitude of complex correlation in front of river mouths in the experiment with constant density has nothing to do with the river runoff. Obviously, these mesoscale features are a result of complex coastal line and bathymetry, which acts almost in the same way in the two experiments. This could be used as a demonstration that even in this very simple case (constant density) impact of wind on the circulation is not trivial.

The role of baroclinicity is well illustrated in the difference between figure 8b and c. Overall, in the presence of density stratification the correlation decreases, which is actually more pronounced in the zonal than in the meridional component (data not shown). The role of density changes when we analyse non-tidal residual currents compared to the case when we include tidal oscillations in the correlation analysis. This is consistent with the approach taken by Kundu (1976), who removed tidal oscillations from his analysis. The general trend for non-tidal residual currents is a decrease of their correlation with wind in the realistic run compared to the constant density run, while the trend derived from the analysis of the total currents is not so simple. This gives an indication that in the presence of tides the instantaneous velocity field could show a rather complicated response to wind forcing.

The explanation of the difference between plots from the two experiments in figure 8b and c is facilitated, if we analyse the differential Eulerian time-mean velocity (figure 9). Overall, the increase of mean velocity in the central part of the model area due to density is comparable to the Eulerian time-mean residual velocity (see figure 7). Furthermore, change in the direction of currents from the realistic experiment to the one with constant density is such that density tends to deflect current velocity in the interior of the model area to the right. On the contrary, in the coastal zone opposite deflection is observed.

The spatial variability of correlation between surface current and wind is indicative for the work done by wind. From the numerical simulations it is obvious that this measure of mechanical forcing is quite complex. It is highly dependent on density, with corresponding patterns changing dramatically over short distances. Most of these changes occur in the coastal zone covered by HFR observations presented in section 2.1. This gives us the motivation to further investigate the consistency between observations and numerical simulations focusing on regional patterns.

4 Model-data comparison

4.1 Time series

To illustrate the typical characteristics of zonal and meridional surface velocity data from HFR observations in direct comparison with model simulations, several 24 h time series examples are shown in figure 10. Velocity components from two locations at two days (one relatively calm, the other one relatively stormy) are displayed. Oscillations of zonal velocity are larger than the ones of meridional velocity giving an initial expectation for the zonal elongation of tidal ellipses in the examined area. Obviously, zonal velocity identifies a clear dominance of M2 signal, which persists both during calm and stormy weather. The temporal variability of meridional component is much less regular, and in contrast to the zonal component is dominated by higher than M2 frequencies.

The low signal level in the meridional velocities explains the relatively large differences between observations and simulations, particularly under stormy weather. The comparison between observations demonstrates that the temporal variability during calm and stormy weather is quite different, which is explained by the large magnitude of the meridional wind component (figure 5). However, the zonal wind velocity is even larger, but it does not substantially affect the tidally dominated zonal current.

The comparison also demonstrates that in location A almost the same characteristics of tidal variability dominate the periods of calm and stormy weather. In contrast, the shapes of the simulated curves in location B during the two analysis periods are quite different. The same applies to the observation data, however in a different way. Obviously, any analysis of tidal ellipses will be strongly dependent upon irregular oscillations in the meridional velocity.

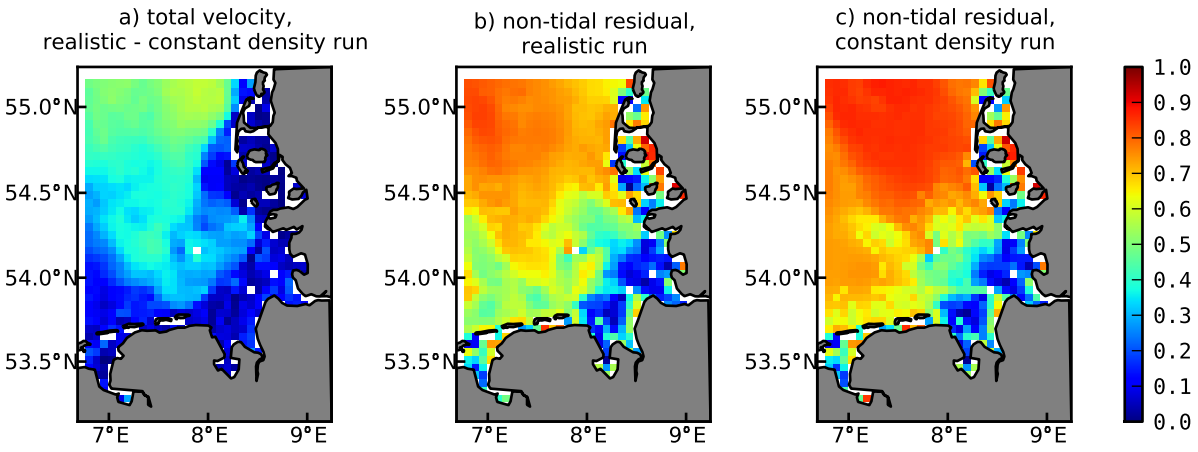

Fig. 8 Magnitude of complex correlation $|\rho|$ of different numerical simulation surface velocities with wind. From left to right, the numerical simulation data is: a) the difference between total surface velocity in the realistic and constant density runs, b) the non-tidal residual surface velocity in the realistic run and c) the non-tidal residual surface velocity in the constant density run.

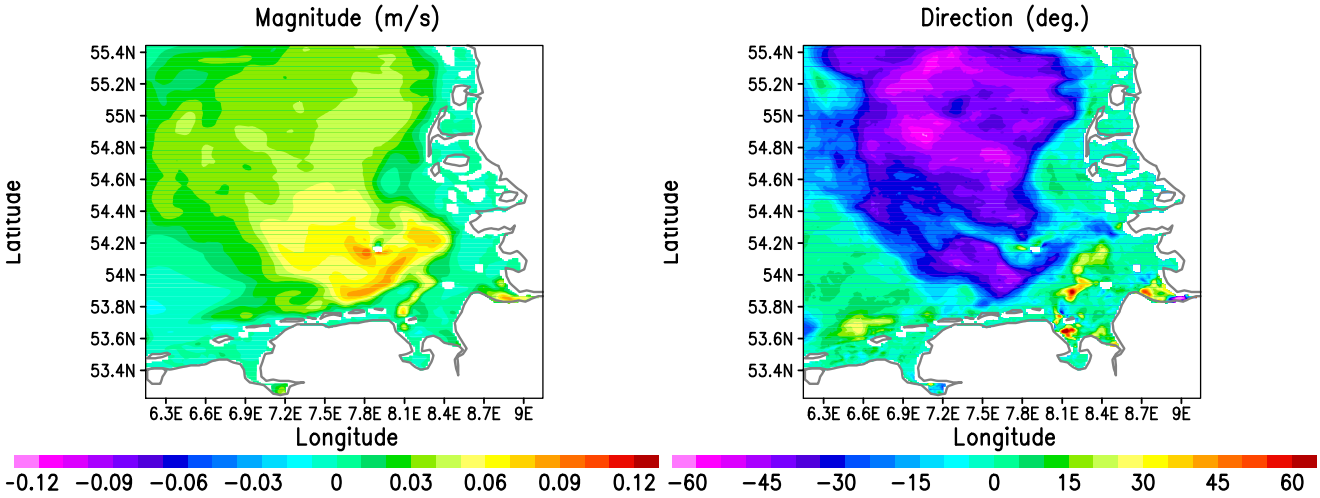

Fig. 9 Difference between Eulerian time-mean velocity magnitude and direction in two experiments (realistic run minus constant density run), magnitude in ms^{-1} and direction in degrees color-coded according to the colorbars.

The above result supports the speculation that the local dynamics are quite complex and selectively sensitive to wind, which gives the major motivation to analyse the local diversity of the sensitivity of circulation to wind forcing.

As a measure of average mismatch over time, the root mean square (RMS) deviation between numerical simulations and HFR observations is shown in figure 11 for the month of 1991/09. Areas of high deviations in the order of $0.2\,\mathrm{ms}^{-1}$ to $0.3\,\mathrm{ms}^{-1}$ are visible near the coast at the eastern as well as south-eastern edge of the observation grid. It is noteworthy that along the line connecting the two radars meridional velocity shows relatively bad agreement (see also Barth et al., 2010). The relatively low values of the RMS deviation (substantially lower than the amplitude of oscillations at least in the zonal direction) support the following analyses.

4.2 M2 tidal ellipsess

Although preliminary studies had prompted the additional implementation of WLS (taking into account HFR observation error estimates) in the tidal analysis routines, the differences to the OLS analyses were negligible for the area and dominant constituents discussed here. Results are therefore shown only for the OLS analyses.

Tidal ellipses for the M2 constituent calculated from observation and model data for the month of September, 1991, are compared in figure 12. Semi-major axis values are on the same order of magnitude for both data sources, with the HFR observations generally offering slightly higher values. From north to south, ellipses degenerate to an almost exclusively zonal movement, more prominent in the HFR observations due to

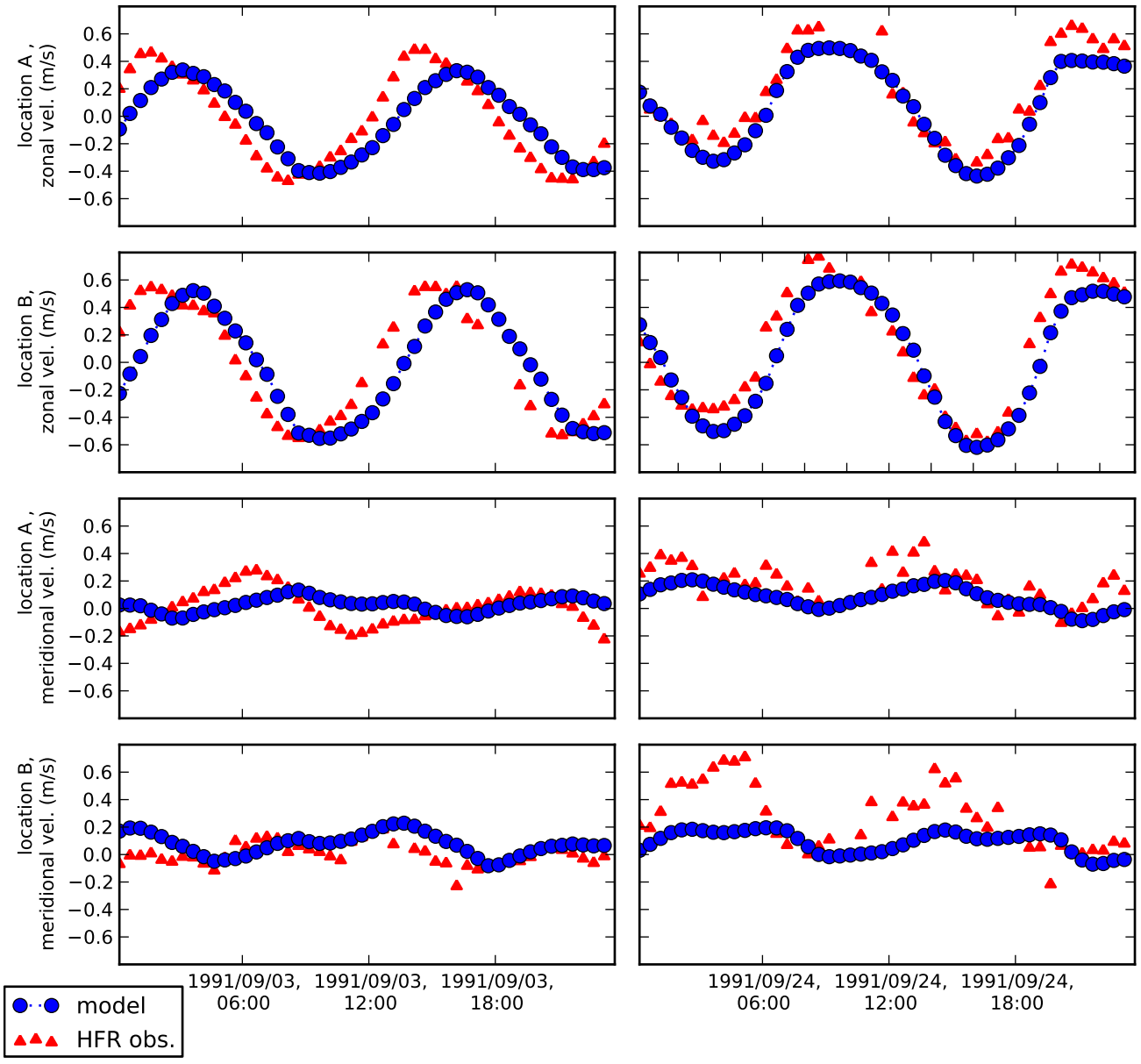

Fig. 10 Time series examples of the zonal and meridional components of the surface velocity (m/s) for HFR observations (red triangles) and model simulations (blue circles). From top to bottom, the panels show: meridional velocity at location A, meridional velocity at location B, zonal velocity at location A and zonal velocity at location B (see figure 2 for location identification). The left panels show timeseries examples for 1991/09/03, a (relatively) calm day, the right panels for 1991/09/24, a stormy day (see figure 5 for wind data at these times).

a much stronger meridional component in the northern half of the region of interest. Here, eccentricity is also systematically lower for the HFR observations, in many areas combined with a shift in orientation away from the zonal towards the meridional axis when compared to the model data. In the south-eastern corner of the region (towards the region of freshwater influence of the Elbe), a shift towards a north-west / south-east orientation is visible in both data sources, but more pronounced in the model output. Here, a region of clockwise rotation is also present in both data sources, although with a clearly larger extent in the model data. A smaller region of clockwise rotation north-east of Helgoland is visible only in the model data. Changes of el-

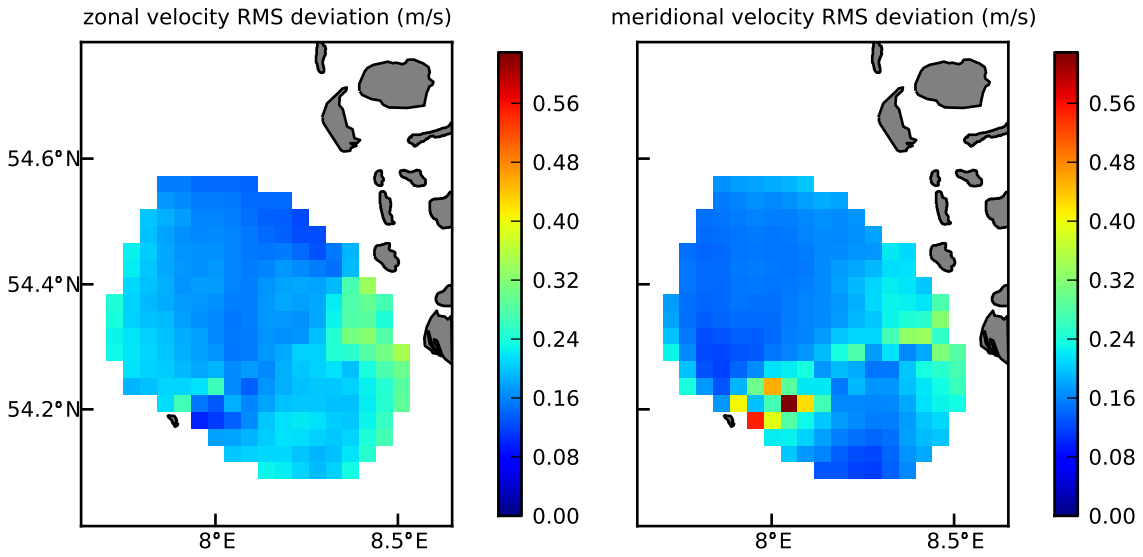

Fig. 11 RMS deviation between numerical simulations and HFR observations for the month of 1991/09, shown separately for the zonal and meridional velocity components, color-coded according to the colorbar.

lipse parameters appear smooth on this spatial scale for both data sources, with slightly more abrupt changes present in the HFR observations north-east of Helgoland as well as west of St. Peter-Ording.

4.3 Wind

The magnitude of complex correlation $|\rho|$ of surface currents with ECMWF wind data for the month of September, 1991, is shown in figure 13, separately for total and non-tidal residual currents based on HFR observations as well as full model output (also interpolated to the observation grid for comparison). For the model data the prominent structure is a meridional gradient clearly visible in non-tidal residual currents and less so in total currents. For the HFR observations, although a similar gradient seems present, it is overlaid by decreasing correlation magnitude at all edges of the observation grid as well as near the HFR system locations. It is plausible that the former could be attributed to data availability and quality (see figs. 2 and 4), the latter to GDOP (see figure 3).

As should be expected, calculating $|\rho|$ based on the synthesised tidal current prediction results in consistently lower values for all data sources (data not shown). The calculation of ρ for HFR total currents versus wind was also carried out for ECMWF data at one grid point further south (54.0° N, 8.0° E instead of 54.5° N, 8.0° E), but did not result in appreciable differences in patterns of magnitude or phase angle (data not shown).

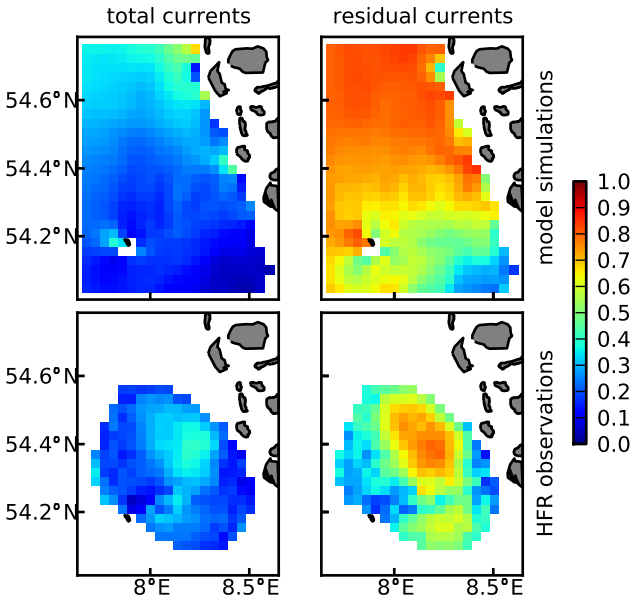

Fig. 13 Magnitude of complex correlation $|\rho|$: total currents (left column) and non-tidal residual currents (right column) for HFR observation data (top row) and model simulations (bottom row). All correlations were calculated versus ECMWF wind data. Only data for the month of September, 1991, was analysed, leading to a maximum possible number of samples per grid point of 120 (6-hourly wind data).

For the non-tidal residual currents, the calculation of $|\rho|$ was repeated for four subsets of the time series, selected based on the wind direction. The four subsets of corresponding wind vectors are shown in figure 14, while the resulting maps of $|\rho|$ based on model simu-

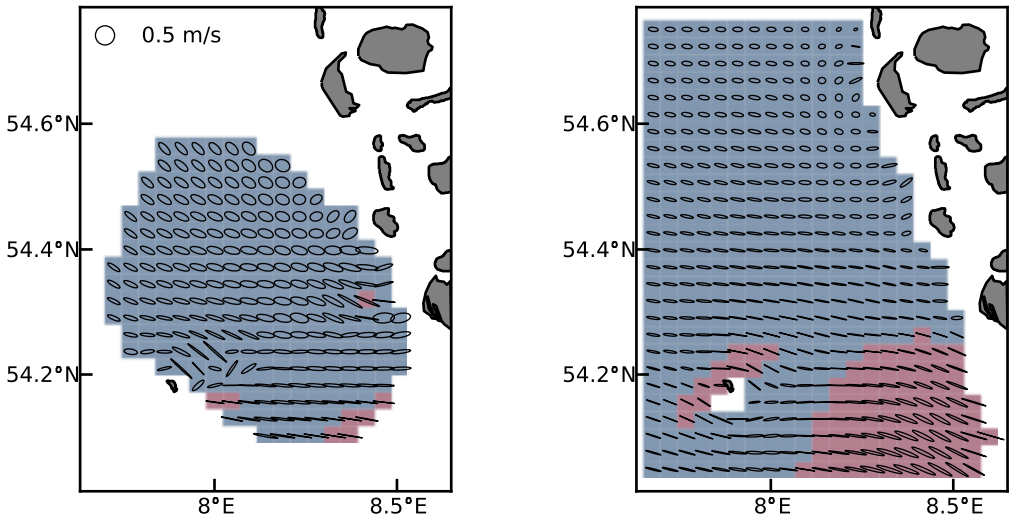

Fig. 12 Dominant tidal ellipses (M2 frequency) derived from HFR observations (left panel) and model simulations (right panel). The sense of rotation of the ellipses is color-coded, blue representing counterclockwise (positive ellipticity) and red clockwise (negative ellipticity) rotation. Analysis based on one month of data (1991/09) at intervals of 30 minutes (1440 samples in time for observation grid points with full coverage over time).

lations as well as HFR observations are shown in figure 15.

The highest similarity to the corresponding map in figure 13 can be found in the subset of eastward wind, paired by high magnitudes of the corresponding wind vectors as seen in figure 14. Higher values of $|\rho|$ for the subset of northward wind visible in the model simulation data are not visible in the HFR observation data. The prominent contrast between higher values north of the baseline connecting the two HFR systems and lower values south and south-east is visible in almost all subsets. A notable exception is the subset of southward wind of the HFR observations, where high values are also visible south of the baseline. The very small sample sizes of these subsets (eastward: 57, northward: 18, westward: 19, southward: 26 samples) is clearly a limiting factor for the significance of this approach with this data.

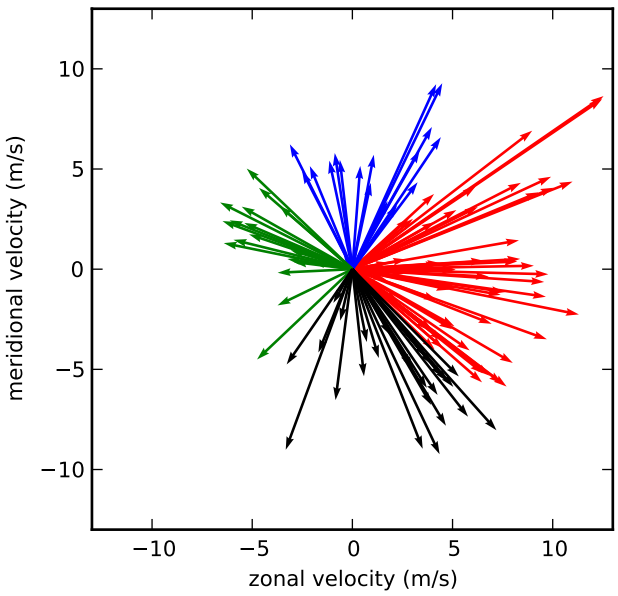

Fig. 14 Wind vectors (ECMWF) for 1991/09, split into four bins based on direction: eastward (red), northward (blue), westward (green) and southward (black).

5 Discussion

When examining HFR surface current observations, the highly non-random patterns in time and space of a) missing values as well as b) the magnitude of observation error estimates pose challenges for different types of subsequent analyses. For example, missing data may often be caused by radio frequency interference. For a nearby site (70 km further north) and similar operating frequencies (25 MHz and 30 MHz), Essen et al. (1983) reported a recurring reduction in HFR range by up to a factor of two. This reduction follows the daily cycle of the ionosphere, which causes problems to the anaysis of other daily variations, e.g. in the wind field. HFR observation error estimates include measurement errors and variability within the coherent integration

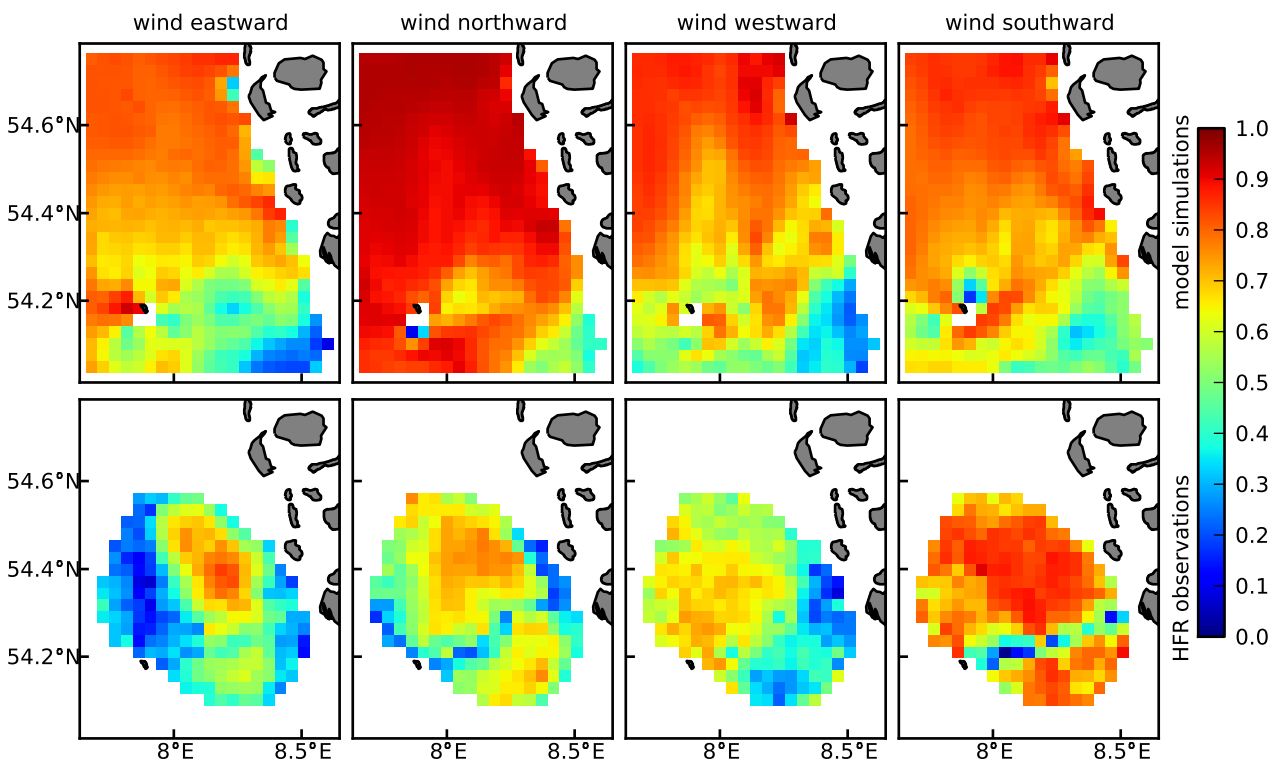

Fig. 15 Magnitude of complex correlation $|\rho|$ split based on wind direction: based on non-tidal residual currents from model simulations (top row) and HFR observations (bottom row), all samples in time separated into four bins according to the wind direction (see figure 14). All correlations were calculated versus ECMWF wind data. Only data for the month of September, 1991, was analysed.

time, as well as a fixed GDOP based on the radar installation geometry. Due to GDOP, the expected dominant spatial pattern in a setup with two HFR system locations is relatively simple, with a rough approximation of one symmetry axis along the baseline and another along a line perpendicular to it and intersecting in the middle between the two HFR systems. Additionally, the error in the surface current measurement increases with range, because of a decreasing Signal-to-Noise-Ratio (SNR). These idealized patterns are visible in the data examined here, but clearly overlaid with patterns which depend on factors other than the geometric setup on an idealized horizontal plane. The interaction between these factors cannot easily be predicted and therefore comparisons with results from a numerical model are very instructive.

The phase lag between numerical simulations and observations has been demonstrated previously. In a recent study, (Barth et al., 2010) showed that optimizing the tidal boundary values via non-sequential assimilation of HFR observations may alleviate this problem to a substantial degree. Higher short-term variance in the HFR observations as well as regular occurence of higher absolute velocities remain an issue for analyses as well as assimilation purposes.

For the tidal analysis of current observations like the HFR data presented here (sampling interval and record length versus noise level, etc.), neither the WLS nor the IRLS approach resulted in large changes in estimated parameters compared to OLS. Note that a) only the dominant tidal constituent was examined in detail and that b) possible improvements in parameter estimation uncertainty were also not part of the comparison between HFR observations and model simulations. An interesting question for further study is the possible degree of similarity between the HFR observation error estimates (as “fixed weights”) and the weights determined via IRLS, and whether the observation error estimates might be used as first guess weights within an IRLS analysis.

In the region of HFR observations, good agreement is illustrated between amplitudes of major tidal constituents derived from numerical model and observations. Furthermore, a qualitative agreement can also be found between M2 tidal ellipses based on model simulations and HFR observations, with an overall trend of the ellipses degenerating going from north to south. The differences between HFR observations and model simulations seem to be of a similar magnitude as found in other studies in the German Bight (for example Car-

bajal and Pohlmann, 2004, based on CODAR observations south of Helgoland). The baseline connecting the two HFRs lies close to a stretch of shallow water known as "Steingrund" (between the island of Helgoland and the mainland coast east of it), which may play a role in separating these distinct subregions. In the model simulations, a region of negative ellipticity in the direction of the Elbe estuary extends almost northward up to Steingrund and is even more pronounced than in the HFR observations. Possible signals from freshwater influence from the Elbe estuary are difficult to ascertain in these observations (let alone compare with nearby estuaries like Weser or Ems) due to the limited extension of the observation grid. This influence may be examined in future studies of data from ongoing HFR installations, again in comparison with model scenarios. To elucidate possible causes for the model simulations' phase lag (for example inadequate parameterization of bottom friction), independent simultaneous observations of the vertical velocity profiles in addition to HFR surface current observations are highly desirable. One possibility would be a simultaneous ADCP deployment (an approach followed by Davies et al., 2001, among others).

The complex correlation with a wind vector time series shows a pattern somewhat similar to the degenerating M2 tidal ellipses, with the magnitude of correlation decreasing in the south-east direction towards the Elbe estuary. This overall pattern can generally be found in both model simulations as well as HFR observations. Even when comparing only grid points where the observation coverage over time is at least 50%, effects of the GDOP as well as decreasing coverage towards the edge and baseline are likely and hinder a clear interpretation. Even under a dominant tidal forcing, as can be found in the German Bight, wind effects may be substantial, in particular if longer time scales are concerned. Intraannual variability is highly probable and demands further examination based on timeseries of appropriate length, either from historical datasets or ongoing installations.

6 Conclusions

HFR surface current observations in the German Bight from 1991 and numerical model hindcasts from a model setup used in current pre-operational applications were compared. Overall consistency was found in terms of zonal and meridional components of velocity timeseries, ellipse parameters of the dominant M2 tidal constituent as well as mesoscale spatial patterns of the magnitude of complex correlation with wind. This correlation however is quite different for different wind directions giving a proof that the corner of German Bight exhibits a complex dynamics where especially the meridional velocity component is difficult to simulate accurately (see also Barth et al., 2010).

The agreement between observations and numerical simulations gives credibility to sensitivity analyses carried out with the aim to quantify the contribution of different forcing mechanisms to regional dynamics. We demonstrated that the change of the correlation patterns between wind and surface current from the coastal to open ocean are not only due to density. The effect of coastal line and topography are quite pronounced as well.

There are not many observational platforms in the coastal ocean with a good spatial and temporal discretisation and good accuracy. In a parallel research, as well as in Barth et al. (2010) and Schulz-Stellenfleth and Stanev (2010) it is demonstrated that HFR surface current observations could substantially improve estimates on physical state and consequently increase the predictive capabilities of numerical models. In this way they could provide an important component for regional operational oceanography.

References

Backhaus JO (1980) Simulation von Bewegungsvorgängen in der Deutschen Bucht. Dtsch Hydrogr Z 15

Barrick DE, Evans MW, Weber BL (1977) Ocean surface currents mapped by radar. Science 198(4313):138–144

Barth A, Alvera-Azcárate A, Gurgel KW, Staneva J, Port A, Beckers JM, Stanev E (2010) Ensemble smoother for optimizing tidal boundary conditions by assimilation of high-frequency radar surface currents. Application to the German Bight. Ocean Sci 6:161–178

Burchard H, Bolding K (2002) GETM - a General Estuarine Transport Model. Tech. rep., Institute for Environment and Sustainability, ISPRA, Italy

Carbajal N, Pohlmann T (2004) Comparison between measured and calculated tidal ellipses in the German Bight. Ocean Dynam 54(5):520–530

Chapman RD, Shay LK, Graber HC, Edson JB, Karachintsev A, Trump CL, Ross DB (1997) On the accuracy of HF radar surface current measurements: Intercomparisons with ship-based sensors. J Geophys Res 102(C8):18,737–18,748

Czitrom S, Budéus G, Krause G (1988) A tidal mixing front in an area influenced by land runoff. Continent Shelf Res 8(3):225–237

Davies AM, Furnes GK (1980) Observed and computed M2 tidal currents in the North Sea. J Phys Oceanogr 10(2):237–257

Davies AM, Hall P, Howarth MJ, Knight PJ, Player RJ (2001) Comparison of observed (HF radar and ADCP measurements) and computed tides in the North Channel of the Irish Sea. J Phys Oceanogr 31(7):1764–1785

Dick S, Eckard K, Müller-Navarra S, Klein H, Komo H (2001) The operational circulation model of BSH (BSHcmod) - model description and validation. Berichte des Bundesamtes für Seeschifffahrt und Hydrographie (BSH) 29, BSH

Essen HH, Gurgel KW, Schirmer F (1983) Tidal and wind-driven parts of surface currents, as measured by radar. Ocean Dynam 36(3):81–96

Flather RA (1976) A tidal model of the north-west european continental shelf. Mem Soc R Sci Liège, ser 6 10:141–164

Janssen F, Schrum C, Backhaus J (1999) A climatological data set of temperature and salinity for the Baltic Sea and the North Sea. Ocean Dynam 51(0):5–245

Kundu PK (1976) Ekman veering observed near the ocean bottom. J Phys Oceanogr 6(2):238–242

Leffler KE, Jay DA (2009) Enhancing tidal harmonic analysis: Robust (hybrid l-1/l-2) solutions. Continent Shelf Res 29(1):78–88

Maier-Reimer E (1977) Residual circulation in the North Sea due to the M2 tide and mean annual wind stress. Ocean Dynam 30(3):69–80

Pawlowicz R, Beardsley B, Lentz S (2002) Classical tidal harmonic analysis including error estimates in MATLAB using t_tide. Comput Geosci 28(8):929–937

PRISMA (1994) Prozesse im Schadstoffkreislauf Meer-Atmosphäre: Ökosystem Deutsche Bucht. BMFT-Projekt 03F0558A1 (1.1.1990 - 31.10.1993). Abschlussbericht, ZMK-Universität Hamburg

Schirmer F, Essen HH, Gurgel KW, Schlick T, Hessner K (1994) Local variability of surface currents based on HF-radar measurements. In: Sündermann J (ed) Circulation and Contaminant Fluxes in the North Sea, Springer-Verlag Berlin Heidelberg

Schulz-Stellenfleth J, Stanev E (2010) Statistical assessment of ocean observing networks - a study of water level measurements in the German Bight. Ocean Mod 33(3-4):270–282

Soulsby R (1983) The bottom boundary layer of shelf seas. In: Johns B (ed) Physical Oceanography of Coastal and Shelf Seas, vol Volume 35, Elsevier, chap 5, pp 189–266

Staneva J, Stanev E, Wolff JO, Badewien T, Reuter R, Flemming B, Bartholomä A, Bolding K (2009) Hydrodynamics and sediment dynamics in the German Bight. a focus on observations and numerical modelling in the East Frisian Wadden Sea. Continent Shelf Res 29:302–319